

## PERIODIC FLOW AND HEAT TRANSFER USING UNSTRUCTURED MESHES

J. Y. MURTHY\* AND S. MATHUR

*Fluent Inc., 10 Cavendish Court, Centerra Resource Park, Lebanon, NH 03766, U.S.A.*

### SUMMARY

A numerical scheme has been developed for computing fluid flow and heat transfer in periodically repeating geometries. Unstructured solution-adaptive meshes are used in a cell-centred finite volume formulation. The SIMPLE algorithm is used for pressure–velocity coupling. For periodic flows the static pressure is decomposed into a periodic component and one that varies linearly in the streamwise direction. The latter is computed from the imposition of overall mass balance at the periodic boundary. A subiteration between the periodic pressure correction equation and the correction to the linear component is used. For heat transfer a formulation using the physical rather than the scaled temperature is employed. The scheme is applied to both laminar and turbulent computations of periodic flow and heat transfer in a variety of heat exchanger geometries; comparison with published computations and experimental data is found to be satisfactory. © 1997 John Wiley & Sons, Ltd.

*Int. J. Numer. Meth. Fluids*, **25**: 659–677 (1997)

No. of Figures: 14.    No. of Tables: 4.    No. of References: 30.

KEY WORDS: periodic flow; periodic heat transfer; unstructured mesh; finite volume; pressure-based; heat exchangers

### 1. INTRODUCTION

Periodic flow and heat transfer occur widely in a variety of industrial applications. In compact heat exchangers, for example, it is common to augment heat transfer by using arrays of fins.<sup>1</sup> In evaporators, elaborate beading and embossment patterns are frequently used to increase surface area and to promote mixing.<sup>2</sup> In condenser tubes, periodically interrupted fins are sometimes used to destroy the integrity of the refrigerant film and promote heat transfer. In other areas such as electronics cooling, electronic components are frequently modelled as infinite arrays of heat generating blocks to facilitate analysis.<sup>3</sup> Periodically arranged turbulators are used in turbine blade cooling passages to enhance heat transfer.<sup>4</sup> In many applications of industrial interest the geometries involved are quite complex and the periodically repeating domains are not simple blocks.

Computational fluid dynamics (CFD) has been used extensively to analyse periodic flow and heat transfer. Patankar *et al.*<sup>5</sup> generalized the concept of fully developed flow to ducts whose geometry varied periodically in the streamwise direction. The analysis included periodicity with specified temperature and specified flux boundary conditions. For the specified temperature case, an iterative

---

\* Correspondence to: J. Y. Murthy, Fluent Inc., 10 Cavendish Court, Centerra Resource Park, Lebanon, NH 03766, U.S.A.

procedure for computing the dimensionless streamwise bulk temperature gradient was devised. Kelkar and Patankar<sup>6</sup> used a similar discretization to solve an antiperiodic problem for flow and heat transfer in a periodic plate channel. Unlike Patankar *et al.*,<sup>5</sup> they used actual rather than scaled temperature as the dependent variable and greatly simplified the procedure for calculating the streamwise bulk temperature gradient. Sathyamurthy and Karki<sup>7</sup> devised an iterative scheme for the computation of the streamwise pressure gradient; this was used to compute laminar flow over heated blocks in an electronics cooling application in Reference 3. Most of these studies used a staggered mesh arrangement with a control volume discretization. The SIMPLE algorithm<sup>8</sup> was used for pressure velocity coupling.

Most published finite volume schemes in this area employ either regular<sup>3,5,6</sup> or body-fitted<sup>9,10</sup> meshes with a single-block mesh topology. Although a single- or multiblock mesh is adequate for the simple geometries considered above, it is inconvenient to use when realistic heat exchanger geometries such as those described in Reference 1 are to be considered. Finite element schemes that provide greater mesh flexibility have also been published (see e.g. Reference 11).

In the last few years, unstructured mesh methods have been developed which greatly ease mesh restrictions and which permit solution adaption. Unstructured mesh schemes for incompressible flows were developed during the 1980s using the control volume finite element method (CVFEM).<sup>12</sup> This method attempted to marry the geometric flexibility of finite element schemes with the conservation property of finite volume schemes. More recently, researchers have attempted to extend the incompressible flow methodology of Reference 8 to unstructured meshes.<sup>13–16</sup> Here a conservative finite volume formulation is applied to arbitrary polyhedra and the SIMPLE family of algorithms is used. Though these methods continue to evolve, preliminary computations have been shown to match standard benchmarks well.

In this paper we use the finite volume methodology presented in Reference 16 in developing a solution procedure for periodic flow and heat transfer. The procedures in References 5 and 6 are generalized for unstructured solution-adaptive meshes. The method is validated against the published literature and shown to perform satisfactorily.

## 2. FLOW AND TEMPERATURE PERIODICITY

Consider a domain with periodic boundaries separated by a translation vector  $\vec{L}$ , as shown in Figure 1. The two periodic boundaries of the domain are denoted as *periodic* and *periodic shadow* for convenience. This domain represents one of a series of periodic modules translated by  $\vec{L}$ . There may be other periodic boundaries in the domain, but there is no net inflow through any of these

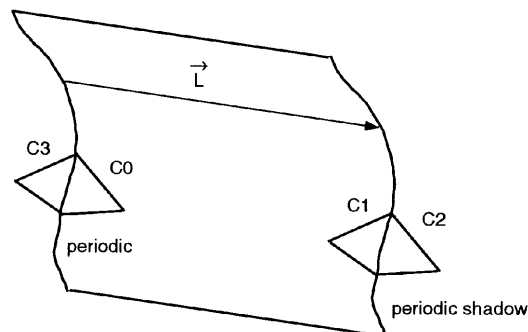


Figure 1. Periodic domain

boundaries. As in Reference 5, we may write the following relationships for the velocity  $u_i$  and the static pressure  $P$  at position  $\vec{r}$ :

$$u_i(\vec{r}) = u_i(\vec{r} + \vec{L}) = u_i(\vec{r} + 2\vec{L}) = \dots, \quad (1)$$

$$P(\vec{r}) - P(\vec{r} + \vec{L}) = P(\vec{r} + \vec{L}) - P(\vec{r} + 2\vec{L}) = \dots. \quad (2)$$

For periodic flows the pressure gradient may be decomposed into two parts—the gradient of a periodic component,  $\partial p/\partial x_i$ , and the gradient of a linearly varying component,  $\beta \hat{e}_L$ :

$$\frac{\partial P}{\partial x_i} = \beta e_{L,i} + \frac{\partial p}{\partial x_i}, \quad (3)$$

where  $e_{L,i}$  is the  $i$ -component of the unit vector  $\hat{e}_L$  in the direction  $\vec{L}$ .

Periodic heat transfer is possible for either Dirichlet or Neumann boundary conditions on temperature. Here the scaled temperature

$$\theta(\vec{r}) = \frac{T(\vec{r}) - T_w}{T_b(\vec{r}) - T_w} \quad (4)$$

is periodic. For Dirichlet boundary conditions on temperature we may write

$$\frac{T(\vec{r}) - T_w}{T_b(\vec{r}) - T_w} = \frac{T(\vec{r} + \vec{L}) - T_w}{T_b(\vec{r} + \vec{L}) - T_w} = \frac{T(\vec{r} + 2\vec{L}) - T_w}{T_b(\vec{r} + 2\vec{L}) - T_w} = \dots. \quad (5)$$

For Neumann boundary conditions the quantity  $T_b - T_w$  is constant across modules. Consequently, we may simplify equation (5) to write

$$T(\vec{r}) - T_b(\vec{r}) = T(\vec{r} + \vec{L}) - T_b(\vec{r} + \vec{L}) = T(\vec{r} + 2\vec{L}) - T_b(\vec{r} + 2\vec{L}) = \dots. \quad (6)$$

Here the bulk temperature  $T_b$  is defined as

$$\frac{\iint_A |u_i e_{L,i}| T \, dA}{\iint_A |u_i e_{L,i}| \, dA} = 0, \quad (7)$$

where  $A$  is the area of cross-section.

### 3. GOVERNING EQUATIONS

The equations for conservation of mass, momentum and energy for the incompressible, steady flow of a Newtonian fluid are

$$\frac{\partial}{\partial x_i}(\rho u_i) = 0, \quad (8)$$

$$\frac{\partial}{\partial x_j}(\rho u_i u_j) = -\frac{\partial p}{\partial x_i} - \beta e_{L,i} + \frac{\partial}{\partial x_j} \left( (\mu + \mu_t) \frac{\partial u_i}{\partial x_j} \right) + F_i, \quad (9)$$

$$\frac{\partial}{\partial x_i}(\rho u_i c_p T) = \frac{\partial}{\partial x_i} \left[ \left( k + \frac{\mu_t}{\sigma_h} \right) \frac{\partial T}{\partial x_i} \right] + S_h. \quad (10)$$

$F_i$  contains those derivatives of the stress tensor not included in the diffusion term in the momentum equations; it may also contain the contributions of body forces consistent with the periodicity of the flow. To sustain periodicity, all fluid properties must be independent of temperature, though they may

have a periodic spatial variation. The energy source term  $S_h$  must also be temperature-independent and spatially periodic; non-zero values are permissible for Neumann boundary conditions only. Turbulence is computed using the high-Reynolds-number  $k-\varepsilon$  model<sup>17</sup>

$$\frac{\partial}{\partial x_i}(\rho u_i k) = \frac{\partial}{\partial x_i} \left[ \left( \mu + \frac{\mu_t}{\sigma_k} \right) \frac{\partial k}{\partial x_i} \right] + G_k - \rho \varepsilon, \quad (11)$$

$$\frac{\partial}{\partial x_i}(\rho u_i \varepsilon) = \frac{\partial}{\partial x_i} \left[ \left( \mu + \frac{\mu_t}{\sigma_\varepsilon} \right) \frac{\partial \varepsilon}{\partial x_i} \right] + C_{1\varepsilon} \frac{\varepsilon}{k} G_k - C_{2\varepsilon} \rho \frac{\varepsilon^2}{k}. \quad (12)$$

The turbulence viscosity  $\mu_t$  is computed as<sup>17</sup>

$$\mu_t = C_\mu \rho k^2 / \varepsilon. \quad (13)$$

The two-layer low-Reynolds number model described in Reference 18 is also implemented.

#### 4. NUMERICAL METHOD

We describe briefly important components of the numerical method used to discretize the governing equations. Details may be found in Reference 16. Cartesian velocities are used as the basis of the flow formulation. For heat transfer we use the temperature directly as the dependent variable, instead of using  $\theta$  as done in Reference 5.

##### 4.1. Domain discretization

The domain is discretized into arbitrary unstructured convex polyhedra. All transport variables are stored at cell centres. The governing equations are integrated over the polyhedron. Consider the differential equation for transport of a scalar quantity  $\phi$ :

$$\frac{\partial}{\partial x_i}(\rho u_i \phi) = \frac{\partial}{\partial x_i} \Gamma \frac{\partial \phi}{\partial x_i} + S_\phi. \quad (14)$$

Integration and discretization about the control volume C0 shown in Figure 2 yields

$$\sum_f J_f \phi_f = \sum_f D_f + (S_\phi \Delta V)_0, \quad (15)$$

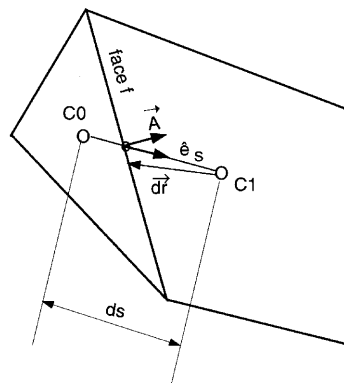


Figure 2. Control volume

where  $J_f$  is the mass flow rate defined as

$$J_f = \rho_f \vec{A}_f \cdot \vec{V}_f. \quad (16)$$

$\vec{A}_f$  is the outward-pointing area vector at face  $f$ .  $D_f$  is the diffusive flux entering C0 through face  $f$  and the summations are over all the faces of the control volume. Thus

$$D_f = (\Gamma \nabla \phi)_f \cdot \vec{A}_f. \quad (17)$$

For the face  $f$  between control volumes C0 and C1 in Figure 2 the diffusive flux can be written as

$$D_f = \left( \Gamma_f \frac{\phi_1 - \phi_0}{ds} \frac{\vec{A}_f \cdot \vec{A}_f}{\vec{A}_f \cdot \hat{e}_s} \right) + \left( \bar{\nabla} \phi \cdot \vec{A} - \bar{\nabla} \phi \cdot \hat{e}_s \frac{\vec{A}_f \cdot \vec{A}_f}{\vec{A}_f \cdot \hat{e}_s} \right). \quad (18)$$

Here  $\hat{e}_s$  is the unit vector along the line joining the cell centroids. The primary gradient (the first term on the RHS of the above equation) is treated implicitly. The secondary gradient (the second term on the RHS) is zero for orthogonal quadrilateral/hexahedral meshes and for equilateral triangular/tetrahedral meshes. It is computed explicitly. The derivative  $\bar{\nabla} \phi$  at the face is taken to be the average of the derivatives at the two adjacent cells. The above treatment is the equivalent of a second-order scheme for structured meshes.

The face value  $\phi_f$  used in computing the convective flux can be taken to be the value at the upwind cell, yielding a first order scheme. To achieve second order accuracy, a linear reconstruction procedure similar to that of Barth and Jespersen<sup>19</sup> is used to write the face value in terms of values in the upwind cell:

$$\phi_f = \phi_{\text{upwind}} + \nabla \phi_{\text{upwind}} \cdot \vec{dr}, \quad (19)$$

where  $\vec{dr}$  is the vector directed from the centroid of the upwind cell to the centroid of the face.  $\nabla \phi_r$  is the reconstruction gradient of  $\phi$  evaluated using the divergence theorem:

$$\nabla \phi_r = \frac{\alpha}{\Delta V} \sum_f (\bar{\phi}_f \vec{A}_f), \quad (20)$$

where  $\bar{\phi}_f$  is the average of the values of  $\phi$  at the adjacent cells and  $\alpha$  is a factor used to ensure that the reconstruction does not introduce local extrema. The limiter proposed by Venkatakrishnan<sup>20</sup> is used in the present work. The gradients used in the diffusion term in equation (18) are computed by applying the divergence theorem with the reconstructed face values  $\phi_f$ .

It is necessary to account for periodicity in computing cell derivatives and reconstruction gradients and in the limiting procedures. For velocity and the periodic pressure component  $p$  this is straightforward. For temperature, equations (5) and (6) are used to evaluate the temperature in the cells in neighbouring modules, as explained in the subsections that follow.

#### 4.2. Boundary conditions

In addition to cell centres,  $\phi$  is also stored at boundary face centroids. The boundary diffusion flux can then be linearized in the same manner as at an interior face, i.e., using equation (18). For the boundary face in Figure 3 this yields

$$D_f = \Gamma_f \frac{\phi_b - \phi_0}{db} \frac{\vec{A}_f \cdot \vec{A}_f}{\vec{A}_f \cdot \hat{e}_b} + \nabla \phi_0 \cdot \vec{A} - \nabla \phi_0 \cdot \hat{e}_b \frac{\vec{A}_f \cdot \vec{A}_f}{\vec{A}_f \cdot \hat{e}_b}, \quad (21)$$

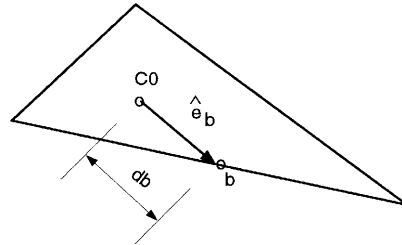


Figure 3. Boundary control volume

where  $\phi_b$  is the value at the boundary and  $\hat{e}_b$  is the unit vector directed from the cell centroid to the boundary face centroid.

For Dirichlet boundary conditions, equation (21) is used to express the boundary diffusion flux as a linear function of the cell and boundary values of  $\phi$ . It is also used to compute the boundary flux of  $\phi$  for postprocessing. For Neumann boundary conditions the prescribed boundary flux of  $\phi$  is included directly in the flux balance for the boundary cell. Equation (21) is then used to compute  $\phi_b$ . This boundary value is used for computing cell gradients during reconstruction as described above, and for postprocessing.

At periodic boundaries the cells C0 and C1 in Figure 1 are considered to be neighbours and share a common periodic face. Thus appropriate neighbour values for pressure and velocity are known. The treatment of temperature is described in a later subsection.

The discretization procedure leads to a set of linear equations relating the value of  $\phi$  at the cell centre to its cell neighbours:

$$a_p \phi_p = \sum_{nb} a_{nb} \phi_{nb} + b. \quad (22)$$

Here  $nb$  is the number of cell neighbours. The above equation is underrelaxed, as described in Reference 8. As in Reference 8,  $a_p > 0$  in the above equation.

#### 4.3. Linear solver

The number of cell neighbours in equation (22) is arbitrary for an unstructured mesh. Consequently, familiar line-iterative solvers and their cyclic variants, e.g. the cyclic tridiagonal matrix algorithm (TDMA),<sup>5</sup> cannot be used. Instead, the system is solved using an algebraic multigrid procedure<sup>21</sup> which constructs coarse level equations by clustering a fine level cell with a neighbour for which the influence coefficient is the highest. The agglomeration procedures are applied across periodic boundaries. A variety of multigrid cycles such as the V-, W- and Brandt cycles have been implemented. For the examples in this paper the V-cycle is used for pressure and the Brandt cycle for all other variables. A Gauss-Seidel relaxation procedure is used at each multigrid level. The procedure is applied across periodic boundaries.

#### 4.4. Discretization of the momentum equation

The periodic pressure  $p$  and the Cartesian components of velocity,  $u_i$ , are stored at cell centres. The momentum equation (9) is discretized using the procedure described. The periodic pressure gradient is computed using linear reconstruction. The linear component of the gradient,  $\beta$ , is either given or assumed temporarily known and is integrated in the same manner as the term  $S_\phi$ . Boundary conditions are also treated as described above.

#### 4.5. Discretization of continuity equation

The continuity equation(8) is integrated over the control volume in Figure 2. A scheme similar to that of Rhie and Chow<sup>22</sup> is used to interpolate pressure to the cell face and to avoid pressure checkerboarding. We define the face mass flow rate as

$$J_f = \rho_f \vec{A}_f \cdot \vec{V}_f - \frac{\rho_f \bar{\Delta} \mathcal{V}}{\bar{a}_p} \left( \frac{p_1 - p_0}{ds} - \bar{\nabla} p_f \cdot \vec{e}_s \right) \frac{\vec{A}_f \cdot \vec{A}_f}{\vec{A}_f \cdot \vec{e}_s}. \quad (23)$$

Here  $\vec{V}_f$  is the average value of velocity at the face and  $\bar{a}_p$  is the average of the cell coefficients  $a_p$ . The second term is a third-order added dissipation which prevents checkerboarding. The linear pressure gradient  $\beta$  appears in  $\vec{V}_f$  as the momentum-averaged value of  $\beta \hat{e}_L \cdot (\vec{A}_f / |\vec{A}_f|)$ .

The discrete continuity equation is written as

$$\sum_f J_f = 0. \quad (24)$$

We use a procedure similar to the SIMPLE algorithm<sup>8</sup> to solve for pressure and velocity. If the momentum equation (9) is solved with guessed values of the pressure gradients  $\partial p^* / \partial x_i$  and  $\beta^*$ , the resulting mass flow rate  $J_f^*$  on face  $f$  does not satisfy the discrete continuity equation (24). We propose a correction  $J'_f$ , i.e.

$$J_f = J_f^* + J'_f, \quad (25)$$

such that the corrected flow rate  $J_f$  satisfies equation (24). Further, we postulate that

$$J'_f = -d_{1,f}(p'_1 - p'_0) - d_{2,f}\beta', \quad (26)$$

where

$$d_{1,f} = \frac{\rho_f \bar{\Delta} \mathcal{V}}{\bar{a}_p ds} \frac{\vec{A}_f \cdot \vec{A}_f}{\vec{A}_f \cdot \vec{e}_s}, \quad (27)$$

$$d_{2,f} = \frac{\rho_f \bar{\Delta} \mathcal{V}}{\bar{a}_p} \vec{A}_f \cdot \hat{e}_L. \quad (28)$$

Substituting equations (25) and (26) into equation (24) yields the pressure correction equation

$$a_p p'_p = \sum_{nb} a_{nb} p'_{nb} + \beta' \sum_f d_{2,f} + b. \quad (29)$$

Here, as in Reference 8,  $a_{nb} = d_{1,f}$  and  $a_p = \sum_{nb} a_{nb}$ . The term  $b$  is the net mass inflow  $\sum_f J_f^*$ . We see that the correction to the linear pressure gradient,  $\beta'$ , appears in the correction equation for the periodic pressure  $p$ .

#### 4.6. Computation of $\beta$

Periodic flows may be computed either for a specified streamwise pressure gradient  $\beta$  or for a specified mass flow rate  $M$ . If  $\beta$  is given, it is used as a known quantity in equation (9), and  $\beta'$  is set equal to zero in equations (26) and (29). However, for many problems of practical interest,  $M$  is given and  $\beta$  must be computed.

In order to find  $\beta$ , we enforce overall mass balance. If the momentum equation (9) is solved with a guessed value  $\beta^*$ , the resulting mass flow rate through the periodic boundary,

$$M^* = \sum_{pf} J_f^*, \quad (30)$$

does not satisfy overall mass balance. We require that the sum of all corrected face flow rates through the periodic boundary be equal to the desired flow rate  $M$ :

$$\sum_{pf} J_f = M. \quad (31)$$

Here,  $pf$  denotes the set of periodic faces. Using (25) and (26), we may write

$$\beta' = - \frac{M - M^* + \sum_{pf} d_{1,f}(p'_1 - p'_0)}{\sum_{pf} d_{2,f}}. \quad (32)$$

The corrections  $p'_0$  and  $p'_1$  are associated with the cells that lie on either side of the periodic boundary. Equations (29) and (32) are solved alternately until convergence.

Once the corrections  $p'$  and  $\beta'$  are obtained, the face flow rate  $J_f^*$  is corrected using equation (25). Cell pressure and  $\beta$  are corrected using

$$\beta = \beta^* + \alpha_b \beta', \quad (33)$$

$$p_p = p_p^* + \alpha_p p'_p. \quad (34)$$

For the co-located scheme used here, it is useful to correct cell velocities  $u_i^*$  computed from the momentum equation

$$u_i = u_i^* - \frac{\sum_f (A_{f,i} p'_f) + \Delta \mathcal{V} \beta' e_{L,i}}{a_p^i}. \quad (35)$$

Here,  $a_p^i$  is the centre coefficient of the momentum equation in the direction  $i$  and  $A_{f,i}$  is the  $i$ -component of the face area vector  $\vec{A}_f$ .

The procedure for the computation of  $\beta$  described above is different from those used in the literature.<sup>3,5</sup> In Reference 5 it is recognized that the Reynolds number is the single governing parameter in the problem; for every  $\beta$  there exists a unique Reynolds number (and *vice versa*). Consequently, a physical property such as viscosity is iteratively changed to impose the correct Reynolds number; the resulting  $\beta$ , suitably non-dimensionalized, is the desired dimensionless streamwise pressure gradient. Kelkar *et al.*<sup>3</sup> describe an iterative scheme for  $\beta$  whereby the velocities  $u_i$  are scaled by a factor  $\gamma = M/M^*$  every iteration to match the imposed flow rate; the factor  $\beta$  is also scaled by  $\gamma^\alpha$  where  $\alpha$  is an underrelaxation factor, typically chosen to be less than unity. The procedure adopted here is similar to that used in parabolized Navier–Stokes solvers to compute the streamwise pressure gradient.<sup>23</sup> It is similar to the procedure described by Kelkar<sup>24</sup> for single-block structured meshes. Here the parameter  $\beta$  is the streamwise pressure gradient, assumed to be aligned with one of the mesh directions,  $\xi$ , of the  $(\xi, \eta)$  system, and  $M^*$  in equation (31) is an average over all  $\xi = \text{constant}$  grid lines.

#### 4.7. Computation of temperature field

The energy equation (10) is discretized using the procedures described previously. Temperature is used as the dependent variable. For cells with periodic or periodic shadow faces, equation (22)



requires temperature in adjacent modules. We describe below the procedure used to obtain neighbour temperature.

*Dirichlet boundary condition.* Here the (same) temperature  $T_w$  is specified on all walls in the domain. For this case the procedure adopted is similar to that in Reference 6. Each iteration of the calculation procedure we compute the factor  $\alpha$  defined as

$$\alpha = \frac{(T_b - T_w)_{pf}}{(T_b - T_w)_{psf}}. \quad (36)$$

Here  $pf$  denotes the set of periodic faces in Figure 1;  $psf$  denotes the periodic shadow faces. The bulk temperature may be considered given at the inflow periodic boundary, say  $pf$ ; thus  $(T_b)_{pf}$  is known. The bulk temperature at the outflow boundary,  $(T_b)_{psf}$ , may be found from equation (7) using existing values of  $T(x, y)$ . Thus  $\alpha$  is nominally known and the temperatures  $T_0$  and  $T_2$  are related by

$$T_2 = \frac{T_0}{\alpha} + \left(1 + \frac{1}{\alpha}\right) T_w. \quad (37)$$

Similarly,  $T_1$  and  $T_3$  are related by

$$T_3 = \alpha T_1 + (1 - \alpha) T_w. \quad (38)$$

The relationships (37) and (38) are used in an implicit manner and modify the coefficients  $a_{nb}$  and  $a_p$  in equation (22). The Dirichlet problem is non-linear, since the eigenvalue  $\alpha$  is not known *a priori* and must be found iteratively as part of the solution.

*Neumann boundary condition.* Consider the case where the heat flux  $q''(x, y)$  enters the domain at the walls; a heat source  $S_h(x, y)$  may also be present. We may compute the change in bulk temperature across the domain,  $\Delta T_b = (T_b)_{psf} - (T_b)_{pf}$  by performing a heat balance for the module:

$$\Delta T_b = \frac{\sum_{wf} q''_f A_f + \sum_c \Delta \mathcal{V} S_h}{\sum_{pf} c_p J_f}. \quad (39)$$

The heat flux is summed over all wall faces ( $wf$ ) in the domain. The heat source is summed over all cells ( $c$ ) in the domain. The relationship between the temperatures  $T_0$  and  $T_2$  may be written as

$$T_2 = T_0 + \Delta T_b. \quad (40)$$

Similarly, the temperatures  $T_1$  and  $T_3$  are related by

$$T_3 = T_1 - \Delta T_b. \quad (41)$$

These relations are incorporated in an implicit manner in equation (22), and modify the term  $b$ .

Unlike the case of Dirichlet boundary conditions, the specified flux problem is a linear one. Furthermore, the formulation given above admits  $T$  and  $T + C$  as solutions, where  $C$  is an arbitrary constant. In practice the temperature level is determined by the specified inlet bulk temperature. To ensure the stability of the multigrid linear solver to round-off, we discard one discrete equation in the algebraic system (22) and replace it with a fixed temperature. After the temperature solution is obtained, all temperatures are scaled using equation (4) to the desired inlet bulk temperature.

#### 4.8. Overall solution procedure

The solution procedure for computing periodic flow is summarized below.

1. Solve the momentum equations with current values of pressure and the streamwise gradient,  $p^*$  and  $\beta^*$ .
2. Compute the face mass flow rates  $J_f^*$ .
3. Iterate between the  $p'$ -equation (29) and the  $\beta$ -correction equation (32) until  $p'$  and  $\beta'$  stabilize.
4. Correct the face flow rate  $J_f^*$  to obtain  $J_f$ . This will satisfy both local and global continuity. Correct  $p^*$  and  $\beta^*$ , as well as the cell-centred velocity  $u_i^*$ .
5. Check for convergence. If unconverged, repeat steps 1–4.

Once a converged flow solution is obtained, the temperature may be computed. The solution procedure for computing the temperature field is summarized below.

1. For the Dirichlet case, compute the eigenvalue  $\alpha$ . For the Neumann case, compute the bulk temperature difference  $\Delta T_b$ ; the latter need be computed only once for the entire calculation.
2. Use  $\alpha$  (or  $\Delta T_b$ ) to compute the modified coefficients and source terms in equation (22).
3. Solve the temperature equation.
4. For Neumann boundary conditions, repeat steps 1–3 until convergence if secondary gradients exist; else the solution is complete. For Dirichlet boundary conditions, repeat steps 1–3 until convergence.
5. For Neumann boundary conditions, scale the temperature to obtain the desired bulk temperature.

#### 4.9. Grid adaption

The solution algorithm described in previous subsections can handle both the traditional  $h$ -refinement<sup>25</sup> as well as grids with 'hanging nodes' resulting from non-conformal grid adaption. In the latter case, cells marked for adaption are subdivided by introducing midpoint nodes at edges and/or cell and face centres. Since the discretization scheme can be used for arbitrary polyhedra, the non-conformal interfaces created by hanging node adaption require no special treatment.

#### 4.10. Non-periodic meshes

Most published work for periodic flow has required that the underlying mesh be periodic. One advantage of admitting arbitrary polyhedra is that non-periodic meshes can be handled easily. Consider the non-periodic mesh shown in Figure 4. The periodic boundary is non-conformal since the faces of cells on either side are not aligned. However, if the non-conformal faces are split into aligned subfaces, the cells on either side of the boundary can be considered to be  $n$ -sided polyhedra (a–b–c–d–e in Figure 4, for example). The procedures outlined above can then be used without modification. Thus it is not necessary to have access to mesh generators capable of generating periodic meshes.

## 5. RESULTS

### 5.1. Fully developed flow in a triangular duct

Flow and heat transfer in triangular ducts are of considerable importance in louvred fin heat exchangers and extensive analyses of this geometry have been published.<sup>26,27</sup> The equations governing fully developed flow and heat transfer are two-dimensional; the axial velocity and a scaled temperature may be solved on the triangle to obtain the velocity and temperature fields. Our intent is to validate the method developed above; consequently, we compute three-dimensional flow and heat transfer using a prismatic domain bounded by two periodic boundaries, as shown in Figure 5. The ducts considered are isosceles; the apex angle is  $2\alpha$ .

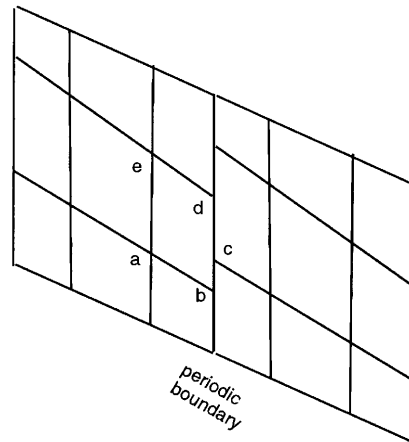


Figure 4. Non-periodic mesh in periodic domain

Because of symmetry, only one half of the cross-section is considered. The domain is discretized using prismatic cells; a typical mesh is shown in Figure 6. The axial mesh is deliberately kept only five cells deep because of the fully developed nature of the flow. A ratio of triangle base to length of 5.0 is used. Mesh sizes range from 648 to 3424 cells in the cross-section, depending on the apex angle. The mesh size employed in each case is listed in Tables I and III respectively.

Computations are performed for  $2\alpha = 20^\circ, 60^\circ$  and  $90^\circ$ . A flow rate is prescribed and the corresponding pressure drop computed using the iterative procedure described above. Both laminar and turbulent flows are considered. For turbulence the two-layer  $k-\varepsilon$  model described in Reference 18 is used. Heat transfer is computed only for laminar flow. Both the specified temperature and the specified heat-flux boundary conditions are considered. For the latter case, the heat flux is assumed to be axially and peripherally uniform.

Tables I and II present the computed  $fRe$  product and Nusselt number respectively for laminar flow.  $Nu_T$  corresponds to the Nusselt number for the specified temperature case;  $Nu_H$  corresponds to that for the specified heat flux case. The computed results compare well with values compiled by Shah and London<sup>27</sup> from a variety of variational, least squares and finite difference solutions in the literature. A typical plot of  $\beta$  versus iteration is shown in Figure 7 for  $2\alpha = 60^\circ$ ;  $\beta$  is found to reach 99% of its converged value within 100 iterations. The local velocity distribution for  $2\alpha = 40^\circ$  is plotted in Figure 8 for different radial lines (corresponding to different values of the angle  $\theta$  shown in

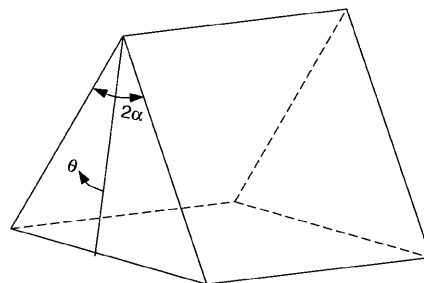


Figure 5. Triangular duct—schematic diagram

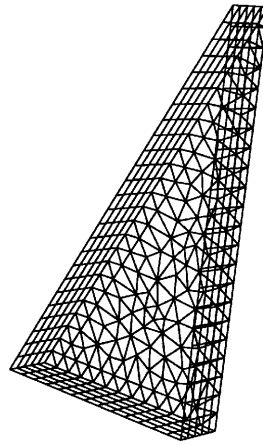


Figure 6. Triangular duct—prismatic mesh

Figure 5). The comparison with a point-matching solution obtained by Sparrow<sup>28</sup> in Figure 8 is good. For turbulent flow the correlation parameter

$$C = 4fRe^{0.25} \quad (42)$$

is tabulated for different values of the apex angle in Table III for  $Re = 10,000$ . Experimental values are interpolated from the data presented in Reference 26. Computed values compare reasonably well with the data.

### 5.2. Flow over a tube bundle

Transverse flow over an in-line tube bundle is computed using the methodology described above. The geometry is shown in Figure 9. The flow is laminar and is governed by the Reynolds number  $Re$  which is defined as

$$Re = \rho DU_m / \mu, \quad (43)$$

where  $U_m$  is the average velocity in the minimum transverse gap between the tubes. Computations are done for two values of the Reynolds number,  $Re = 10$  and  $100$ . A single geometry corresponding to  $S_T/D = S_L/D = 1.25$  is used.

A triangular mesh of 3160 cells is used. Hanging node adaption is used to concentrate cells in regions of high gradient; the resulting mesh is shown in Figure 10. The mass flow rate corresponding to the desired Reynolds number is prescribed and the pressure coefficient, defined as

$$C_p = \frac{\Delta P}{0.5 \rho U_m^2}, \quad (44)$$

Table I. Triangular duct—laminar flow friction factors

$2\alpha$ (deg)	Cross-section grid size	Computed	Shah and London	Difference (%)
20	3424	12.90	12.822	0.65
40	1584	13.31	13.22	0.66
60	1080	13.40	13.33	0.51
90	648	13.174	13.153	0.16

Table II. Triangular duct—laminar flow Nusselt number

$2\alpha$ (deg)	Computed		Shah and London		Difference (%)	
	$Nu_T$	$Nu_H$	$Nu_T$	$Nu_H$	$Nu_T$	$Nu_H$
20	2.07	0.375	2.0	0.366	3.5	2.5
40	2.43	1.42	2.39	1.38	1.7	2.6
60	2.51	1.91	2.47	1.89	1.6	0.8
90	2.38	1.37	2.34	1.34	1.5	2.0

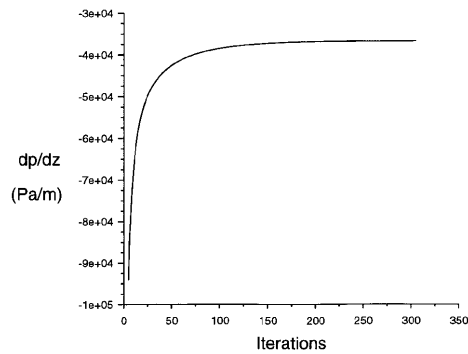
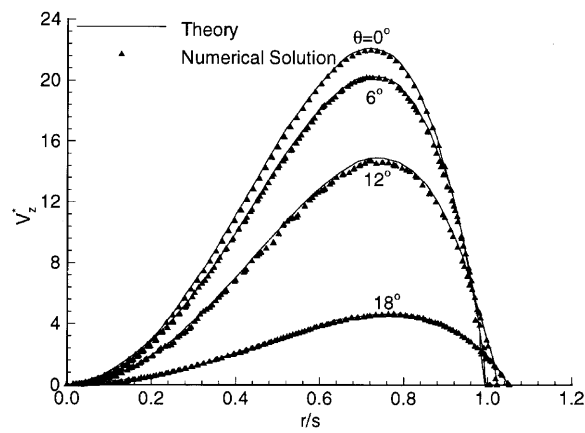
Figure 7. Triangular duct—convergence history for  $\beta$ Figure 8. Triangular duct—axial velocity profiles for  $2\alpha = 40^\circ$ 

Table III. Triangular duct—correlation parameter for turbulent flow

$2\alpha$ (deg)	Cross-section grid size	Computed	Experimental	Difference (%)
20	3424	0.278	0.285	2.4
40	1584	0.283	0.301	6.0
60	1080	0.295	0.301*	2.0

\* Schiller's data

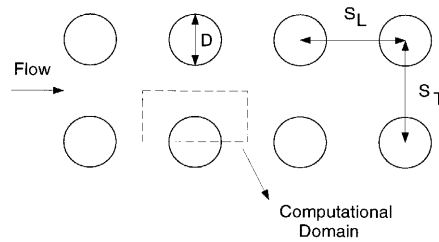


Figure 9. Tube bundle—schematic diagram

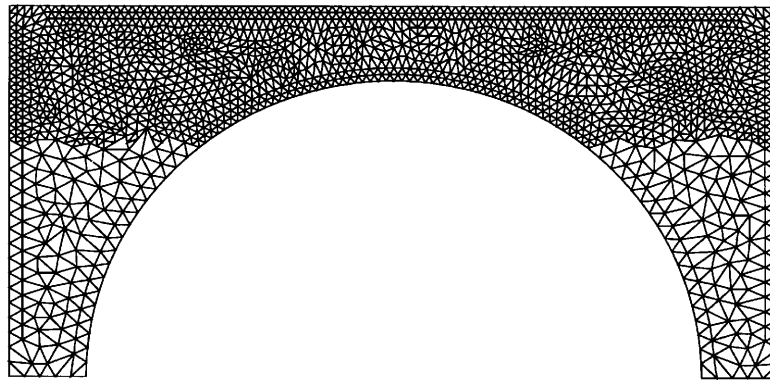


Figure 10. Tube bundle—adapted mesh

computed. Here  $\Delta P$  is the pressure difference resulting from the axial pressure gradient  $\beta$  across a periodic module.

Table IV compares computed values of  $C_p$  with those measured by Antonopoulos.<sup>29</sup> The agreement with experimental data is good.

### 5.3. Flow and heat transfer in a serrated channel

Turbulent flow and heat transfer are computed for periodic flow in a serrated channel. The geometry is shown in Figure 11. Flow enters the domain at a Reynolds number of  $1.2 \times 10^4$  (based on the mid-channel height  $H_m$  and the average mid-channel velocity). A specified heat flux condition is imposed on both the flat and serrated walls. A single geometry corresponding to  $H_s/H_m = 1.0$ ,  $L_s/H_m = 8$  and  $L/H_m = 8.075$  is considered. The objective is to predict periodic flow and heat transfer and to compare predictions with measurements in Reference 30.

Table IV. Tube bundle—comparison of computed  $C_p$  with experiment

$Re$	Computed	Experimental	Difference (%)
10	17.77	17.96	1.06
100	1.949	1.946	0.15

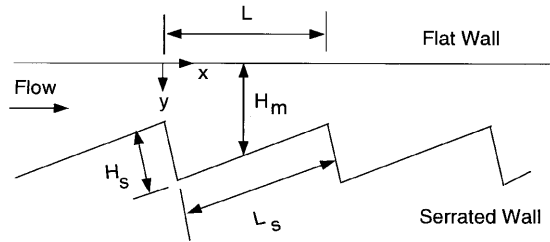


Figure 11. Serrated channel—schematic diagram

The high-Reynolds-number  $k-\varepsilon$  model is employed.<sup>17</sup> The mass flow rate corresponding to the desired  $Re$  is prescribed and the axial pressure gradient computed as a part of the solution. The calculation domain is shown in Figure 12. It consists of quadrilateral mesh of 2400 cells with non-conformal periodic boundaries.

The computed axial velocity  $U/U_m$  is compared with experimental data from Reference 30 in Figure 13. Figure 14 shows a comparison of the local Nusselt number  $Nu$ , with experimental data.  $Nu$  is defined as

$$Nu = \frac{q'' H_m}{k(T_w - T_b)}. \quad (45)$$

The comparison with data is reasonable and of the same order as the  $k-\varepsilon$  model predictions in Reference 30 (not shown).

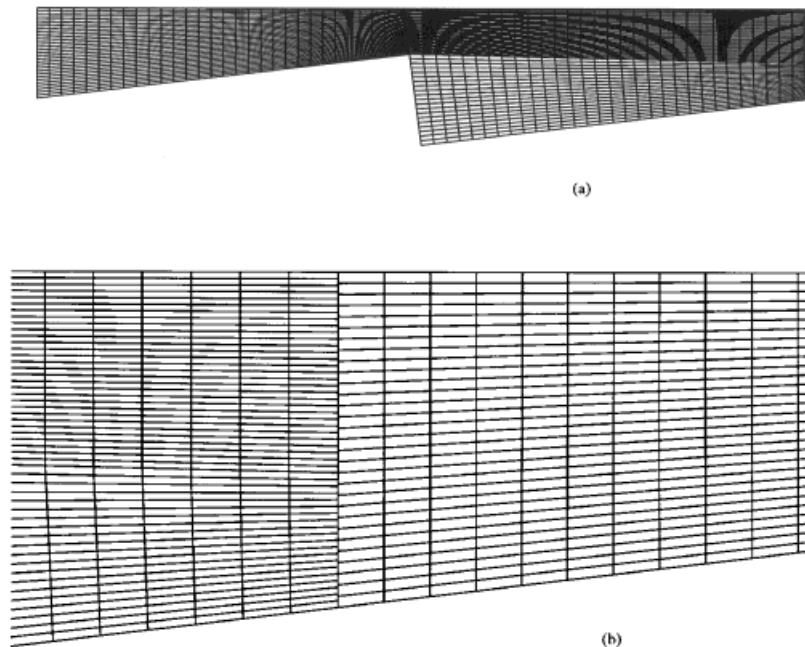


Figure 12. Serrated channel—(a) mesh and (b) detail of periodic boundary

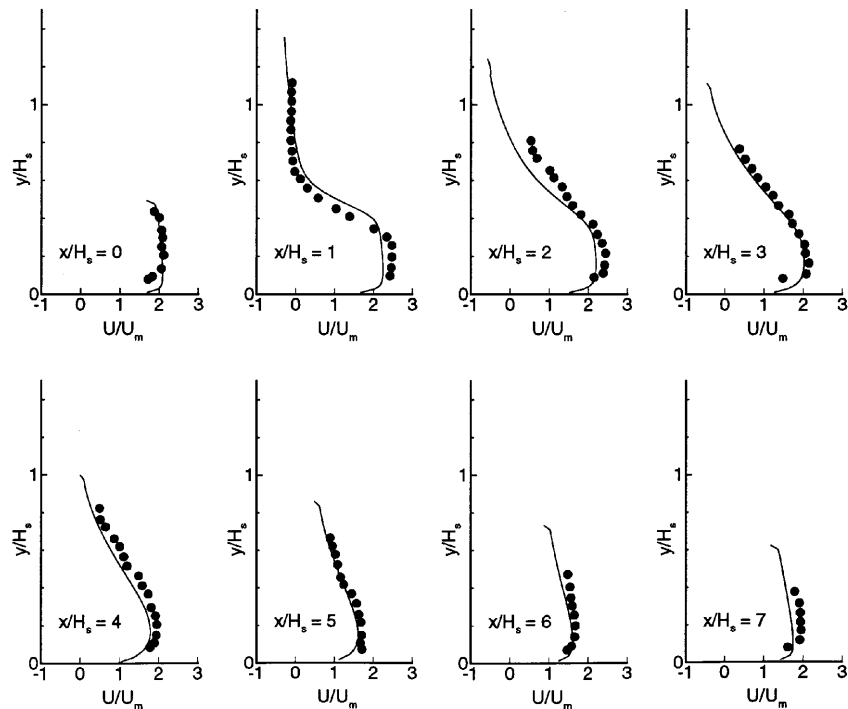


Figure 13. Serrated channel—axial velocity comparisons: ●, experiment; —, computed

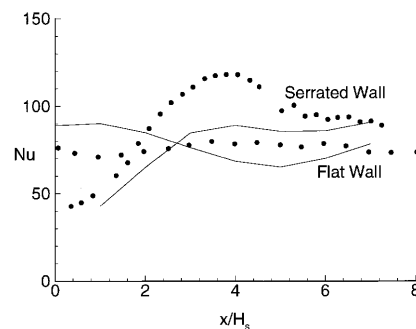


Figure 14. Serrated channel—local Nusselt number distribution: ●, experiment; —, computed

## 6. CLOSURE

A novel conservative finite volume scheme is used to develop a solution procedure for periodic flow and heat transfer in complex geometries. The computational scheme employs unstructured convex polyhedra and admits solution adaption. Previously published formulations for periodic flow are generalized to unstructured meshes. A correction procedure is used for computing the streamwise pressure gradient subject to a mass flow rate constraint. The method is applied to flow and heat transfer in a variety of heat exchanger geometries and its geometric flexibility demonstrated through the use of prismatic, triangular and quadrilateral cells with hanging node adaption and non-conformal



periodic interfaces. Both laminar and turbulent flow problems are computed and good agreement with published numerical and experimental data is found.

#### ACKNOWLEDGEMENTS

We wish to acknowledge the contributions of N. Carter, D. Choudhury, S. E. Kim, J. Maruszewski and G. Spragle of Fluent Inc. to various aspects of this work. The use of Fluent Inc.'s FLUENT/UNS, PreBFC and TGrid codes is gratefully acknowledged.

#### APPENDIX: NOMENCLATURE

$a_{nb}$	neighbour coefficient
$a_p$	neighbour coefficient
$A$	area
$\vec{A}$	area vector
$c_p$	specific heat at constant pressure
$D$	diffusive flux
$F_i$	body force in direction $i$
$G_k$	turbulence production
$J$	mass flow rate
$k$	turbulence kinetic energy, thermal conductivity
$\vec{L}$	periodic translation vector
$M$	imposed mass flow rate
$p$	periodic component of static pressure
$P$	static pressure
$q''$	heat flux
$r$	position vector
$S_h$	heat source
$S_\phi$	source of $\phi$
$T$	temperature
$T_b$	bulk temperature
$T_w$	wall temperature
$u_i$	velocity component in Cartesian direction $i$
$x_i$	co-ordinate direction

#### *Greek letters*

$\alpha$	bulk temperature ratio
$\alpha_p, \alpha_b$	underrelaxation factors
$\beta$	streamwise pressure gradient
$\Gamma$	diffusion coefficient
$\Delta T_b$	bulk temperature rise across module
$\Delta \mathcal{V}$	volume of control volume
$\varepsilon$	turbulence dissipation rate
$\theta$	periodic temperature
$\mu$	molecular viscosity
$\mu_t$	turbulence viscosity
$\rho$	density

$\sigma_h$	turbulence Prandtl number for temperature
$\sigma_k$	turbulence Prandtl number for $k$
$\sigma_\varepsilon$	turbulence Prandtl number for $\varepsilon$
$\phi$	transported scalar

#### Subscripts and superscripts

$f$	face
$nb$	neighbour cells
$pf$	periodic face
$psf$	periodic shadow face
$()^*$	value after solving momentum equation
$()'$	correction

#### Other

$\sum_f$	summation over all faces of control volume
$\sum_{nb}$	summation over all cell neighbours
$\sum_{pf}$	summation over all faces on periodic boundary

#### REFERENCES

1. W. M. Kays and A. L. London, *Compact Heat Exchangers*, 3rd edn, McGraw-Hill, New York, 1984.
2. T. Ohara and T. Takahashi, 'High performance evaporator development', *SAE Tech. Paper 880047*, 1988.
3. K. M. Kelkar, P. S. Sathyamurthy, K. C. Karki and S. V. Patankar, 'Solutions of laminar flow and heat transfer over an array of heated blocks', *ASME Paper 93-WA/EEP*, 1993.
4. Y. M. Zhang, W. Z. Gu and J. C. Han, 'Heat transfer and friction in rectangular channels with ribbed or ribbed-grooved walls', *J. Heat Transfer*, **116**, 58–65 (1994).
5. S. V. Patankar, C. H. Liu and E. M. Sparrow, 'Fully developed flow and heat transfer in ducts having streamwise-periodic variations of cross-sectional area', *J. Heat Transfer*, **99**, 180–186 (1977).
6. K. M. Kelkar and S. V. Patankar, 'Numerical prediction of flow and heat transfer in a parallel plate channel with staggered fins', *J. Heat Transfer*, **109**, 25–30 (1987).
7. P. S. Sathyamurthy and K. C. Karki, *Internal Rep.*, Innovative Research Inc., 1992.
8. S. V. Patankar, *Numerical Heat Transfer and Fluid Flow*, McGraw-Hill, New York, 1980.
9. R. C. Xin and W. Q. Tao, 'Numerical prediction of laminar flow and heat transfer in wavy channels of uniform cross-sectional area', *Numer. Heat Transfer*, **14**, 465–481 (1988).
10. D. Choudhury and K. C. Karki, 'Calculation of fully developed flow and heat transfer in streamwise-periodic dimpled channels', *J. Thermophys. Heat Transfer*, **5**, 81–87 (1991).
11. G. Segal, K. Vuik and K. Kassels, 'On the implementation of symmetric and antisymmetric periodic boundary conditions for incompressible flow', *Int. j. numer. methods fluids*, **18**, 1153–1165 (1994).
12. B. R. Baliga and S. V. Patankar, 'A control-volume finite element method for two-dimensional fluid flow and heat transfer', *Numer. Heat Transfer*, **6**, 245–261 (1983).
13. Y. Jiang and A. J. Przekwas, 'Implicit, pressure-based incompressible Navier–Stokes equations solver for unstructured meshes', *AIAA Paper 94-0305*, 1994.
14. I. Demirdzic and S. Muzaferija, 'Numerical method for coupled fluid flow, heat transfer and stress analysis using unstructured moving meshes with cells of arbitrary topology', *Comput. Methods Appl. Mech. Eng.*, **125**, 235–255 (1995).
15. L. Davidson, 'A pressure correction method for unstructured meshes with arbitrary control volumes', *Int. j. numer. methods fluids*, **22**, 265–281 (1996).
16. S. R. Mathur and J. Y. Murthy, 'A pressure based method for unstructured meshes', *Numer. Heat Transfer*, **31**, 195–216 (1997).
17. B. E. Launder and D. B. Spalding, *Lectures in Mathematical Models of Turbulence*, Academic, London, 1972.
18. S. E. Kim, 'Application of a two-layer zonal approach to computations of complex turbulent flows', in *Turbulent Flows*, FED Vol. 208, ASME, New York, 1995, pp. 75–80.
19. T. J. Barth and D. C. Jespersen, 'The design and application of upwind schemes on unstructures meshes', *AIAA Paper 89-0366*, 1989.
20. V. Venkatakrishnan, 'On the accuracy of limiters and convergence to steady state solutions', *AIAA Paper 93-0880*, 1993.

21. B. R. Hutchinson and G. D. Raithby, 'A multigrid method based on the additive correction strategy', *Numer. Heat Transfer*, **9**, 511–537 (1986).
22. C. M. Rhie and W. L. Chow, 'Numerical study of the turbulent flow past an airfoil with trailing edge separation', *AIAA J.*, **21**, 1523–1532 (1983).
23. S. V. Patankar and D. B. Spalding, 'A calculation procedure for heat, mass and momentum transfer in three-dimensional parabolic flows', *Int. J. Heat Mass Transfer*, **15**, 1787–1805 (1972).
24. K. M. Kelkar, personal communication, 1992.
25. W. A. Smith and K. R. Blake, 'Multigrid solution of internal flows using unstructured solution-adaptive meshes', *Tech. Rep. NAS3-25785*, NASA Lewis Research Center, Cleveland, OH, 1992.
26. W. M. Kays and H. C. Perkins, in *Handbook of Heat Transfer*, McGraw-Hill, New York, 1973, pp. 7-110–7-138.
27. R. K. Shah and A. L. London, *Laminar Flow Forced Convection in Ducts*, Academic, New York, 1978.
28. E. M. Sparrow, 'Laminar flow in isosceles triangular ducts', *AIChE J.*, **8**, 599–604 (1962).
29. K. A. Antonopoulos, 'The prediction of turbulent inclined flow in rod bundles', *Comput. Fluids*, **14**, 361–378 (1986).
30. S. Obi, K. P. Kobayashi, A. M. Bethancourt, H. Yoshida, T. Asano and R. Echigo, 'Experimental and computational study of turbulent heat transfer characteristics in serrated channel flow', *Int. J. Heat Fluid Flow*, **16**, 398–404 (1995).